



# Investigation of the effect of three-point bending testing parameters on the behavior of 3D printed sand

Walid Fekih Ahmed<sup>1</sup> · Mohamed Ben Hadj Sghaier<sup>1</sup> · Samir Allaoui<sup>1</sup>

Received: 23 February 2022 / Accepted: 21 May 2022 / Published online: 30 May 2022  
© The Author(s), under exclusive licence to Springer-Verlag London Ltd., part of Springer Nature 2022

## Abstract

3D sand mold printing allows rapid and direct fabrication of complex-shaped molds and cores that helps to overcome the limitations of conventional casting. The manufactured molds and cores, having complex geometries, are subjected to severe thermomechanical loads during casting and thus must have sufficient rigidity to meet the technical requirements. Therefore, a mastery of their behavior and intrinsic sand properties becomes essential for a better dimensioning of molds and cores but also the simulation of casting processes. The bending is the most critical load type, for sand cores under casting conditions, and therefore needs to be characterized. This study proposes to investigate the effect of testing parameters, which are span-to-thickness and strain rate, on the three-point bending behavior of printed sand. The results showed that the elastic modulus increases with the rise of the span-to-thickness parameter and is not affected by the strain rate. The bending strength, for its part, is only affected by strain rate. The test results and DIC measurement made it possible to give recommendation for the optimal testing parameters.

**Keywords** 3D printed sand · Furan binder · Three-point bending test · Digital image correlation

## 1 Introduction

The 3D printing of molds and cores using binder jet technology makes possible many improvements in casting process. Compared to conventional casting, it provides the capability to fabricate any complex mold and core geometries, which are impossible to obtain without 3D printing, using layer-by-layer deposition without the use of patterns and core box [1, 2]. Indeed, 3D sand mold printing helps to overcome the limitations of conventional casting such as limitations on geometry, providing undercuts and higher lead times due to the pattern making. This technology allows rapid and direct fabrication of complex-shaped molds and cores of custom-made and production of unit pieces.

The design freedom offered by additive manufacturing (AM) combined with the good dimensional accuracies of the obtained parts allows to increase the capability of casting process by the following: the decrease of the required metal

by using hemispherical riser instead of cylindrical riser [3]; improving the casted part quality and dimensional accuracy following the fast and uniform cooling of the casting allowed by the use of shell-truss sand mold [4, 5]; improving the melt flow control that leads to reducing the presence of inclusion by using optimized parabolic and conical-helix sprue [6]; increasing the freedom in design of riser and gating system [7], etc. Additive manufacturing of sand mold has revolutionized the molding industry by allowing weight reductions of complex parts of up to 33% [8], without losing the technical requirements of the component, while reducing inclusions [9] and offering energy savings [10].

However, to achieve these performances, the mechanical behavior of the printed sand must have sufficient rigidity to meet the technical requirements and not too high to avoid generating excessive residual stress that may give casting defects [11, 12]. Several works in the literature have therefore focused on the characterization of the mechanical behavior of printed sands, through classical and non-classical mechanical tests, to identify the intrinsic characteristics of the material and to dimension the molds and cores for foundry applications as accurately as possible. Due to the difficulty in clamping the 3D printed sand specimen on the tensile machine, which is due to the porous nature and brittle

✉ Samir Allaoui  
samir.allaoui@univ-reims.fr

<sup>1</sup> University of Reims Champagne-Ardenne,  
ITheMM EA7548Campus Sup Ardenne,  
08000 EijsinCharleville-Mézières, France

behavior, the most used tests to identify the mechanical parameters are bending test using single prismatic specimen [13, 14], tensile test using dog bone specimens [4], compression using unconfined compressive strength specimen [15, 16], and indirect tensile strength test using the Brazilian test [17, 18].

Three-point bending is the most widely used method for testing the quality of cores and molds prepared with printed sand in the foundry industry. This is due to the technical simplicity of conducting these tests coupled with the need for mechanical performance of the cores in terms of sufficient strength to allow handling and manipulation operations and high bending strength. Indeed, bending is the most critical type of loading, for sand cores under casting conditions, which can be imposed by clamping forces, thermal load, flow drag, and buoyancy loads.

The different results of the literature showed that the final properties and quality of the 3D sand printed mold depend on the printing parameters. A high re-coater speed results in high porosity, which when followed by curing at lower temperatures improves polymerization of resin and increases the evaporation of solvent and hence, the sand particles get tightly packed [14, 19]. Sand compaction, which affects the strength and permeability of the mold and thus the casting quality, is also affected by the orientation and the position of the specimens in the job box [20]. This is due to the layering which strongly affects the behavior of 3D printed sands [17, 18]. This anisotropic behavior of printed specimens is due to more oriented porosity along the direction of printhead movement which impacts the trajectory of the droplet [17]. This anisotropy effect must therefore be considered when defining the mold position in the printer job box.

Another important parameter that has been studied is the layer thickness. Indeed, increasing the layer thickness under the same binder saturation conditions leads to an increase in flexural strength due to improved powder pulverization and binder penetration in the vertical and lateral directions [21]. Finally, concerning the effect of the constituent properties of the printed sand, it has been shown in the literature that increasing the grain fineness index leads to a decrease in mechanical properties while increasing the binder ratio and curing time improves the mechanical properties [15, 16].

In addition to the effect of processes, test conditions and environment also play a non-negligible role on the measured behavior. Indeed, the final properties and quality of the 3D sand printed mold depend on the time and storage conditions prior to testing due to the interaction of the material with the environment and specially with the humidity uptake [13]. The analysis of the results of the different studies shows a difficulty in reproducing the mechanical properties which can be attributed to the porous nature of the printed specimens but also to the testing conditions [22–24] or to test

conditions. Some strategies were proposed to avoid dispersed mechanical properties obtained by three-point bending strength like the use of test with an anti-buckling device [22].

Despite the numerous studies published in this field, the behavior of printed molds remains not fully mastered because of the several parameters influencing the behavior of printed sand.

The studies of the literature highlighted the important effect of the processes and the storage conditions on the behavior of the printed sand but no studies, to our knowledge, address the effect of test conditions. Moreover, the studies use different experimental protocols to carry out the three-point bending tests, which show a significant dispersion of results, making it difficult to compare and cross-reference their results. However, the dimensioning of foundry molds and cores requires the behavior laws and the real intrinsic elastic parameters of the material allowing to have robust numerical simulations.

It is within this framework that this study aims to contribute to the mastery of the printed sands' behavior through the evaluation of the effect of test conditions on the stiffness measured by three-point bending test. Digital image correlation (DIC) technique, which is a contactless method, was used to measure the strain field of sand specimens during tests to analyze the obtained behaviors according to the different conditions.

## 2 Experimental procedure

### 2.1 Materials and method

The three-point bending test specimens were printed, layer-by-layer, by the binder jetting 3D printer ExOne S-Max Machine, which is equipped with  $1800 \times 1000 \times 700 \text{ mm}^3$  job box. The re-coater spread a 280- $\mu\text{m}$  layer of sand premixed with the acid activator on the job box and the inkjet printer head applies a furfuryl alcohol-based binder to the appropriate zone of the layer. A slice of specimen is formed by particle sand bonding within the zone where the binder was applied. The other areas with unbound sand, which will be removed at the end of printing, are used as support for next slices during printing. The job box moves downwards, and a same process continues until the last slice is printed. The recoating speed used for printing the specimens is 150 mm/s with a sand that has an average grain size of silica particles of 140  $\mu\text{m}$  and its standard deviation is 25  $\mu\text{m}$ . The drop frequency of the inkjet printer head is 10 kHz with a print resolution of 0.11 mm and printhead voltage, which controls drop volume, is 79.8 V. All the tested specimens were printed in the “Z” direction to overcome the effect of the printing direction on the characterized mechanical

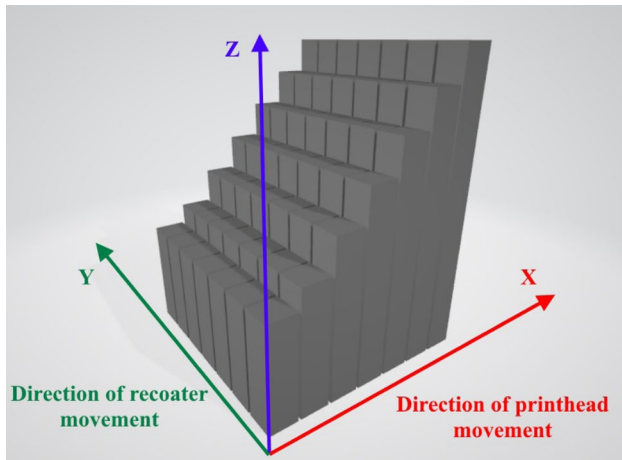


Fig. 1 Printing configuration of the specimens

behavior which has already been characterized in the literature (Fig. 1). The specimens were printed with several lengths but with a 22-mm square cross-section. This cross-section has been chosen because of being the most used in the literature for the bending specimens of printed sand as well as the sand obtained using core box [13, 24] but also the most widely applied for the quality control of sand cores as described by American Foundrymen’s Society [25] and similarly by the German standard VDG [26]. The specimens have an apparent density of  $1315 \pm 7 \text{ kg/m}^3$ .

After printing the specimens, bending tests were performed on a universal testing machine Instron 3366 with a 10 kN load cell. A data acquisition rate of 100 Hz was set using a Bluehill software. The loading and supporting pins of the three-point bending device have a diameter of 10 mm.

Two testing parameters were investigated in this study to highlight their effect on the mechanical behavior of the printed sand: testing speed and the span-to-thickness (length/height) ration. Three-point bending tests were performed at two displacement rate levels (0.05 and 5 mm/min) to investigate the effect of strain rate on the 3D sand printed behavior.

To assess the effect of the span-to-thickness ratio ( $L/h$ ), several configurations were tested. The three-point bending test can give rise to a combined effect of bending and shear behaviors. This combination is governed by the value of span-to-thickness ratio. When it is important one tends to have a pure bending, whereas when it is weak the shear behavior is predominant. Between the two, one obtains a behavior combining pure bending and shearing. Bending tests with different span-to-thickness ratios ( $L/h$ ) were therefore carried out to define a ratio minimizing the shearing effect. Seven distances

between the two supporting pins ( $L$  from 60 to 200 mm) were allowed by the used bending device (Table 1). This range of variation integrates the most used distance in the literature which is 150 mm [13, 20, 24].

The specimen section remained fixed ( $22 \times 22 \text{ mm}$ ); this gives a span-to-thickness ration going from 2.73 to 9.09 (Table 1). The different batches of specimens were printed with length equal to the distance between the two supporting pins ( $L$ ) to which it was added 10 mm overhang on each side (specimen length =  $L + 20 \text{ mm}$ ). Therefore, the specimens are not of the same length. This avoids the parts of the specimen, which are located beyond the supports, generating forces opposite to the applied load and therefore disturbing the result, given the forces reached and the density of the material.

In a general case of three-point bending tests, the deflection is given by the Timoshenko beam theory below:

$$\Delta = \frac{P.L^3}{48.b.D} + \frac{P.L}{4.A.G} \tag{1}$$

where  $\Delta$  is the deflection,  $P$  the applied force,  $b$  the width of the specimen,  $L$  the distance between the two supporting pins,  $D$  the bending stiffness,  $G$  the shear modulus, and  $A$  the section of the specimen.

The resulting behavior is a coupling of pure bending and shear behavior. To measure the bending stiffness, it is necessary to know span-to-thickness threshold value beyond which there is a pure bending configuration, without a coupling with shear, and for which the theory of Euler–Bernoulli beams can be applied. This is one of the objectives of this study which aims to determine this threshold for the case of printed sand. For the sake of simplicity, the elastic modulus ( $E$ ) will be evaluated by the theory of Bernoulli beams in this study because the use of coupling requires a characterization of the shear beforehand whose testing is complex. The bending strength ( $\sigma_{\text{Max}}$ ) and the fracture energy ( $W_{\text{tot}}$ ) are calculated according to continuum mechanics.

In addition, tests were also performed using digital image correlation (DIC) measurements to obtain the strain fields and compare them between different configurations of span-to-thickness ratio ( $L/h$ ). The configurations used for these measurements are those with distance between the two supporting pins of 100, 150, and 200 mm. The principle of DIC is to assess the displacement fields, and thus strain fields, over the surface of a deforming specimen by comparing two images acquired at different steps of deformation. The first image, acquired at the beginning of the test, is used as a reference image and the second one, acquired after

Table 1 Span-to-thickness ratio used for the three-point bending tests

Span length (mm)	60	75	100	125	150	175	200
Span length/thickness $L/h$ (mm)	2.73	3.41	4.55	5.68	6.82	7.95	9.09

some increment of deformation, is the deformed state of the specimen. Prior to applying the measuring process, a region of interest is defined on the reference image and divided into small subsets. The software performs an image correlation by identifying the most similar subset in the deformed image and then calculating the local strain tensor from the spatial distribution of the displacement field for each image.

The stereovision system used is LAVISION Strain Master composed of two CCD (charge coupled device) cameras, which has 5-million-pixel resolution, connected to a computer which allows the acquisition and processing of images via software. Thirty frames per second were saved for each test. Prior the tests, a random pattern is spread on the sample surface with a painting to enhance the image contrast.

All the specimens have been stored after printing and tested at room temperature with a 30–50% relative humidity. The mechanical behavior of the sand varies during the first hours of printing and stabilizes after a few hours [13]. To limit this variability and its effect on the results of this study, a sufficient time to stabilize the behavior and overcome the environment effect has been set at 24 h after production. This also represents the typical time between printing the molds and core and their end usage in foundry practice.

At least three specimens were used for each testing configuration to verify repeatability.

## 2.2 Quality control of the specimens

All specimens were printed in the same direction (direction “Z”) to avoid the anisotropy of the printed sand due to non-uniform resolution of printing. The cross-section dimensions of each specimen were controlled after cleaning to assess accurately the mechanical parameters such as the flexural strength and modulus. The measured dimension tolerances of width and thickness are  $\pm 0.15$  mm and 0.11 mm respectively.

The loss on ignition was used to measure the amount of binder in the printed specimens. To do so, a quantity of printed sand with a mass of about 14 g was extracted from 3D printed specimen, and then put in ceramic crucible and finally heated to calcinate the binder. The procedure followed and the associated measures are described below. The first step of loss on ignition procedure is weighting empty crucible to get its mass  $M_1$ . Then, about 14 g of sand samples is introduced into the crucible and they are weighed again to get total exact mass  $M_2$  of the crucible with sand. The crucible is put in a furnace at 900 °C. After 2 h, the crucible is removed from the furnace and placed in a desiccator for cooling. After cooling, the total mass of the burned-out sand and the crucible is measured again to get mass  $M_3$ .

All of weighing was carried out by a precise balance with an accuracy of  $\pm 0.001$  g. The loss on ignition was determined by the following equation:

$$\text{Loss on ignition (\%)} = 100 \times \frac{M_2 - M_3}{M_2 - M_1} \quad (2)$$

Three measurements for each set of specimens with the same length were performed, and an average of the results has been done. The polymeric binder measured is equal to  $2.033 \pm 0.025\%$  of the mass of the printed sand.

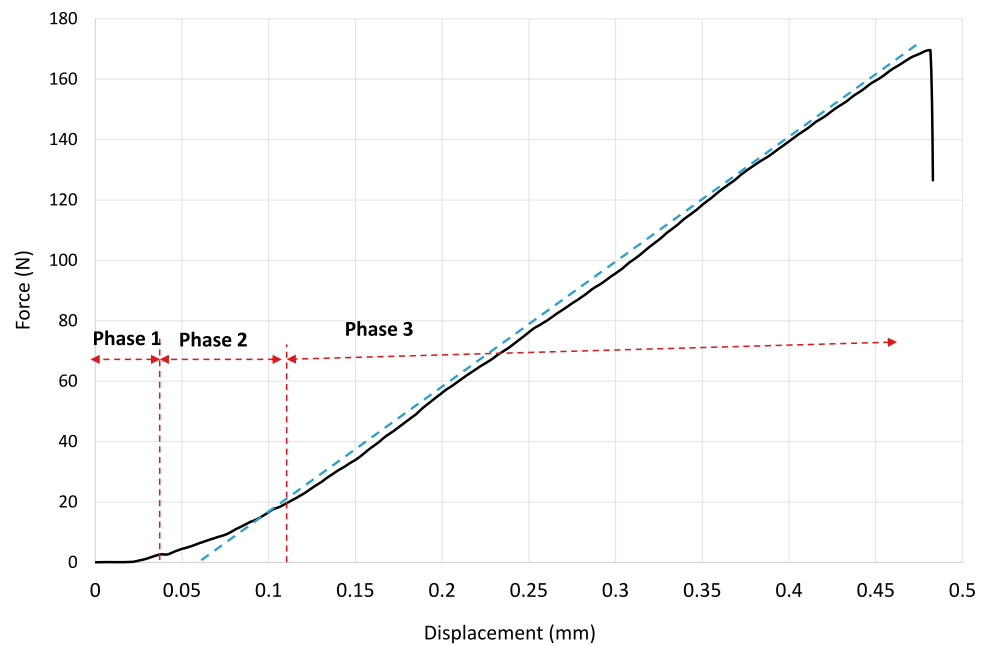
## 3 Results and discussion

An example of the force–displacement curve is given in Fig. 2 for the case of a span length of 150 mm. A change in the slope shown in the figure was observed on all the curves with three distinct phases of the behavior (Fig. 2). The beginning of the bending test (phase 1) is characterized by the crushing and sliding of sand particles located on the specimen surface at the contact zones with the loading and supporting pins. This leads to generates low forces and therefore very low strains at the specimen/device contact areas. This can be observed on the displacement measured by DIC in the loading direction where the most important values, but still weak (less than 0.01 mm), remain localized at the contact area with the loading pin (Fig. 3a). In this phase, variations and instability of the load can occur (Fig. 2) due to the instability of the phenomena and the sliding that occurs. The tested specimen does not undergo bending in this phase considering the very small displacement, which is of the order of the precision of the DIC measurements, measured on the rest of the specimen as well as the lower part of the specimen.

Once local stability between sample and pins is achieved, phase 2 of the behavior begins and the load increases non-linearly (Fig. 2). In this phase, two concurrent phenomena occur simultaneously: bending of the specimen and a local crushing of the material due to Hertz pressure. Indeed, with the increase in the force, we observe a beginning of the specimen bending in this phase characterized by an increase in the deflection. In the state of loading in phase 2 illustrated by Fig. 3b, a deflection of the specimen of the order of 0.024 mm is measured. Part of the machine displacement was not transmitted to the specimen as a whole and was absorbed by the local compression, due to the Hertz pressure, at the contact area with the loading pin where the displacement is 50% greater (displacement of 0.038 mm).

Finally, once this phase is over, phase 3 is entered, characterized by a linear behavior of the material (Fig. 2) and where its deflection increases significantly but always with the presence of compression on the upper part of the

**Fig. 2** Example of load–displacement curve of a specimen with a span length of  $L = 150$  mm



specimen in contact with the device pins (Fig. 3c). To overcome or limit the local crushing due to the Hertz pressure, it would be necessary to favor the use of loading and supporting pins having a large diameter and not use small value as in the literature [13, 19].

The behavior exhibits a brittle fracture that occurs spontaneously at the middle of the specimen when the maximum force is reached (Fig. 4). The fracture initiation is localized at the lower face of the specimen where tensile stress value is maximum, which generates decohesion of sand grains.

The comparison of the force–deflection curves of three-point bending tests performed for different span lengths with a fixed testing speed of 5 mm/min is shown in Fig. 5. For better readability, only one curve per configuration is plotted in the figure. A change in the slope with the presence of the three phases described before is observed for all tests of each configuration. However, while increasing the span length, the extent of phases 1 and 2 decreases and becomes weaker for the configuration like with the spans 175 mm and 200 mm. The curves obtained for these two configurations are also smoother than the others and contain less irregularity in the evolution trend of the force.

All tested configurations exhibit a brittle fracture and a good repeatability of the curve slope illustrated by a maximum dispersion of around 7% of the calculated parameters (Table 2). The configuration with a span length of 75 mm is the one that has the maximum dispersions (7% for the maximal strength and 12% for the fracture energy).

The increase of supporting span value leads to a significant decrease in the maximum force level and an increase

in the deflection value at failure point (Fig. 5). The average values of the bending strength have ranged from 6 to 7 MPa. We observe a low standard deviation for each value (Table 2), with a deviation less than 7%, in contrast to the results reported by previous studies done on three-point bending tests [22] or even the four-bending test [23], where the test conditions are cleaner because they are free of shear, with adapted protocols and setups.

The evolution of the bending strength as function of supporting span seems to be not significant (Fig. 6a), which is not the case for the fracture energy value that was assessed by the integration of the area under the curve. Indeed, the increase of distance between the supporting pins leads to a decrease of fracture energy value of about 24 MJ between the span lengths of 60 and 125 mm (Table 2). From the value of 125 mm, corresponding to a span-to-thickness ration of 5.68, the fracture energy reaches a plateau with a value of around 30 MJ and no longer evolves significant (Fig. 6b).

Concerning the stiffness of the material, it was evaluated by calculating the Young modulus on phase 3 of the bending curves according to Euler–Bernoulli beam theory instead of the Timoshenko beam theory as discussed before. The results show good repeatability with a maximum variation of 10% obtained for the span length of 60 mm (Table 2). The elastic parameter seems to increase continuously, without stabilizing, with the span length evolution. To confirm this trend, loading–unloading tests were performed with the different configurations to have more reliable measures.

Figure 7 represents a typical load–displacement response of a loading–unloading bending test with hysteresis

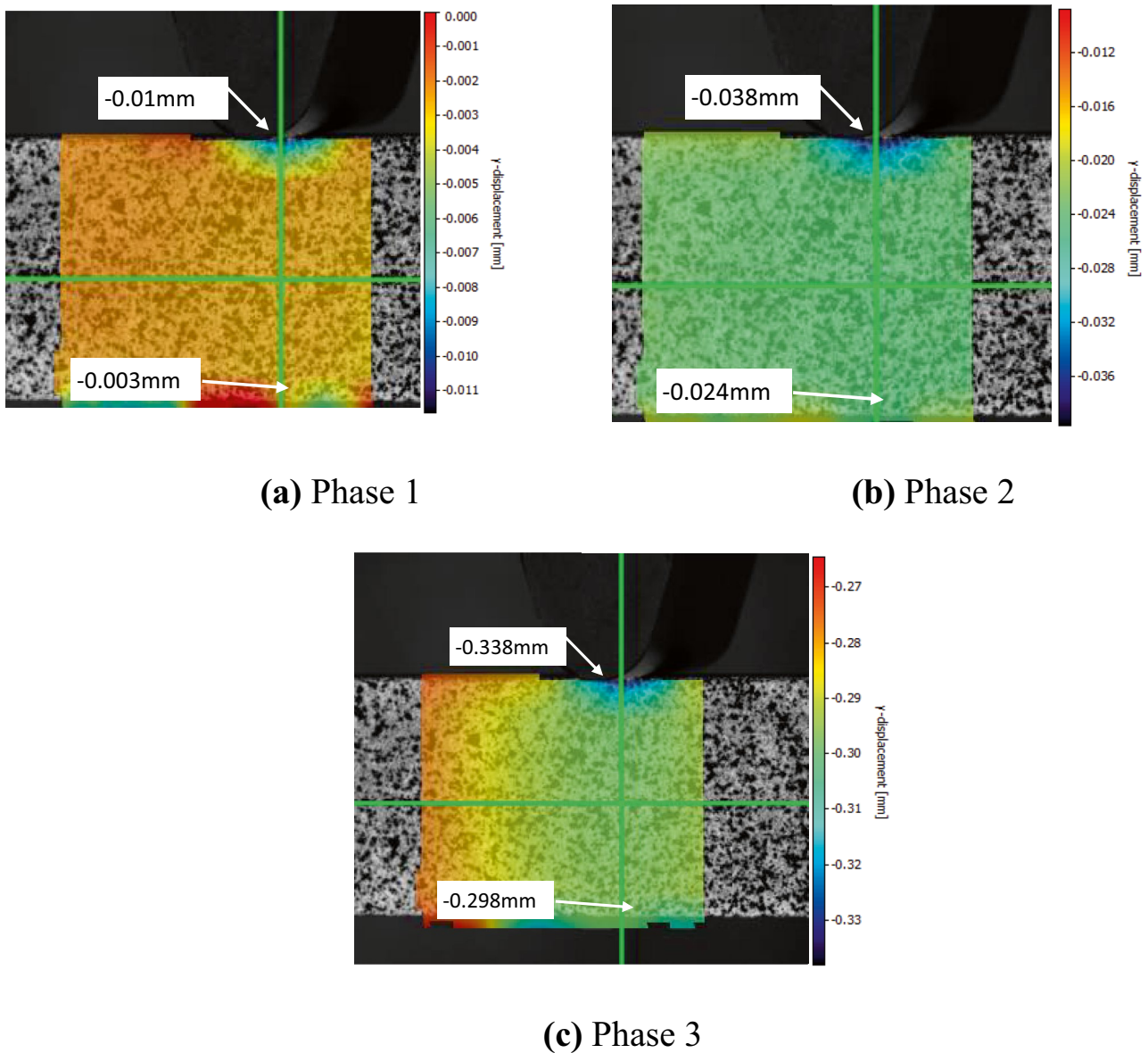
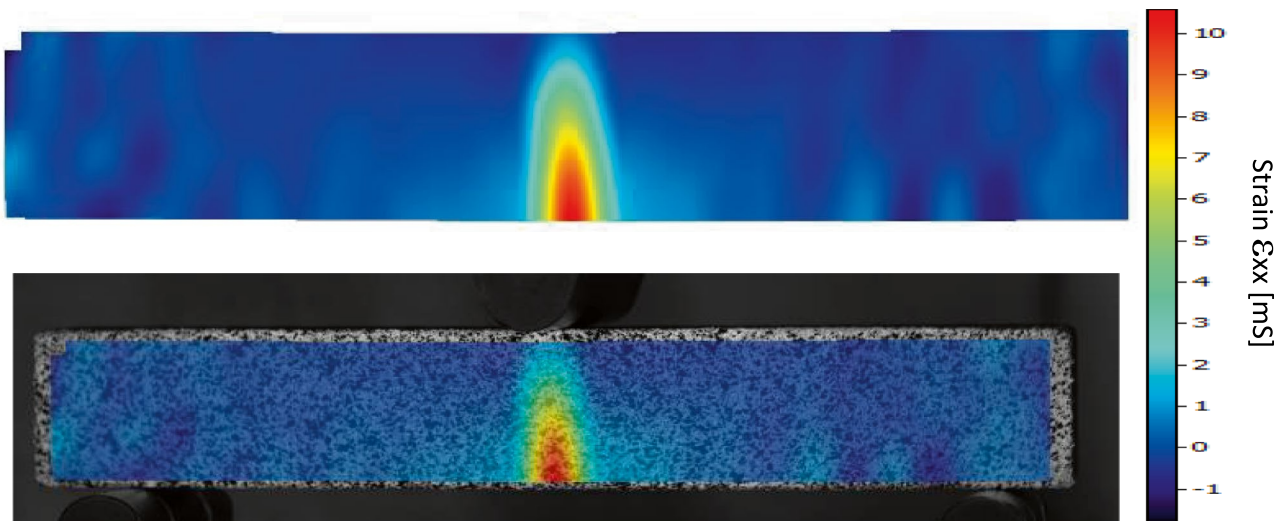


**Fig. 3** Displacement fields in the loading direction of the specimen during testing. **a** Phase 1. **b** Phase 2. **c** Phase 3

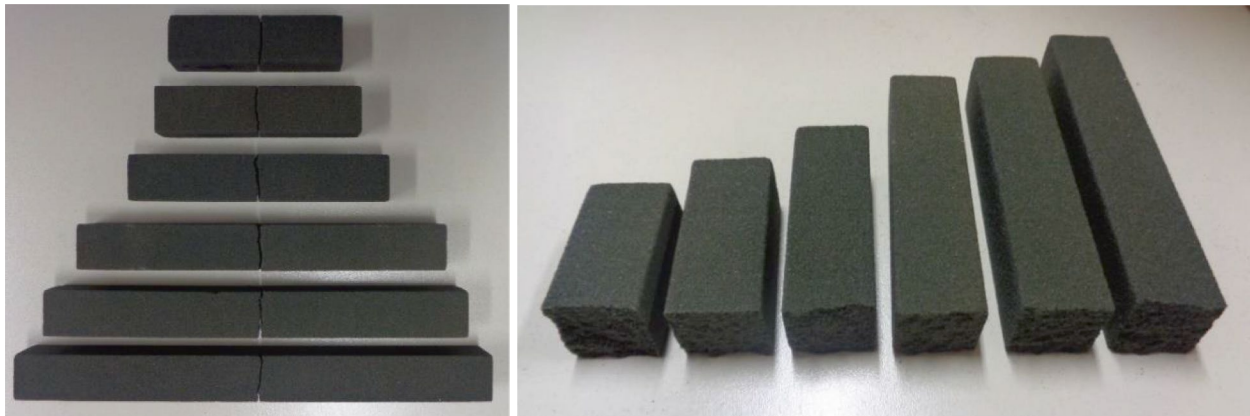
phenomenon. Five cycles uniformly distributed as function of imposed load were carried out for each test. The response of load–displacement of each cycle shows elastic and plastic behaviors of 3D printed specimen until fracture, which reflect the elastic behavior of binder and irreversible sliding of sand particles, respectively. The elastic modulus values were evaluated on the unloading parts of the curves in the linear region. For each test, several values were measured on the unloading phases of the elastic behavior. An average value of the Young modulus, as well as the standard deviation, was established for each span length configuration and is presented in Fig. 8. In the same figure, the evolution of

the Young modulus evaluated directly on the linear part of the bending curves is plotted for comparison.

The first remark which can be made is that the values of the Young modulus evaluated during the loading–unloading tests are greater and with less dispersion (maximum variation of 1.3%) than those evaluated with the conventional bending tests (Fig. 8). We reach a ratio of 3.2 and 1.3 times between the two configurations respectively for the span lengths of 60 mm and 200 mm. This deviation between the values measured by the two methods decreases with the increase of span length. This difference can be explained by the fact that the evaluation of the elastic moduli during the



(a) Strain field ( $\epsilon_{xx}$ ) distribution during the specimen failure



(b) failure surfaces of the specimens

**Fig. 4** Failure of the specimens. **a** Strain field ( $\epsilon_{xx}$ ) distribution during the specimen failure. **b** Failure surfaces of the specimens

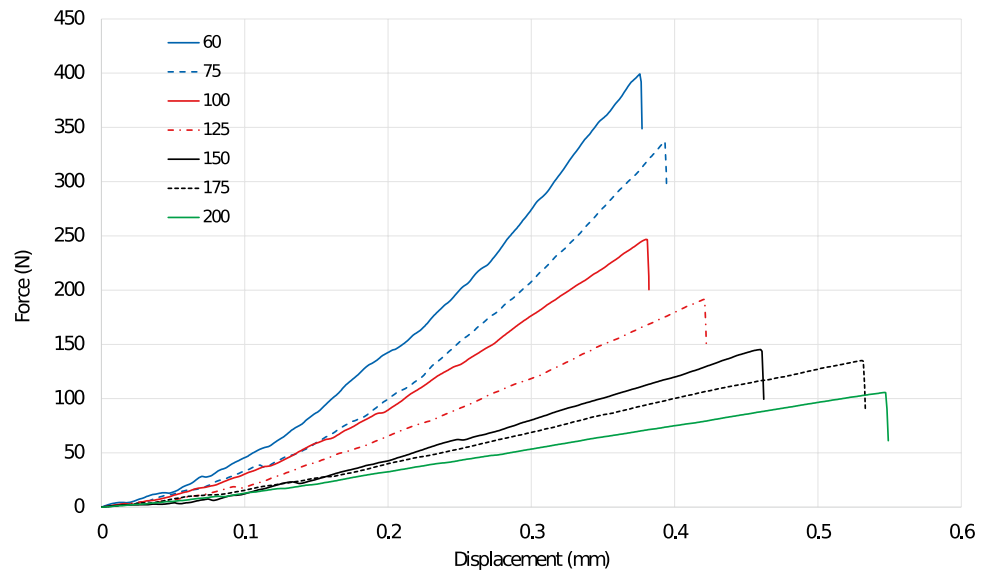
loading–unloading tests, which are more realistic, makes it possible to overcome the effect of local compression, due to Hertz pressure, at the contact zones between specimen and the pins.

Elastic modulus increases with increasing span length. However, for those measured during loading–unloading tests, we reach a plateau at a span length of 175 mm, corresponding to a span-to-thickness ratio of 7.95, where the value stabilizes around 2400 MPa (Fig. 8) that indicates that the pure bending is reached after this. Remember that the evolution of fracture energy reached a plateau starting from

a span-to-thickness ratio of 5.68 corresponding to a span length of 125 mm. Consequently, for the characterization of the bending behavior of sand using three-point bending tests, it will be appropriate to choose a span-to-thickness ratio greater than 8 to overcome the coupling with the shear behavior and the parasitic phenomena, related to the specific behavior of sand or the experimental conditions, which occur during the three-bending test.

Indeed, given its composition, sand can be considered a composite material and therefore a heterogeneous material. Its mechanical behavior is therefore governed by the

**Fig. 5** Load–displacement curves of the printed specimen at different distances between supports



combination of those of its constituents. Given the modest values of the stresses reached during the tests, the sand grains will tend to be animated by a rigid body movement and not to deform, because of their great rigidity, while the binder which is a polymer will deform. These mechanisms will occur at the local (microscopic) scale of the material.

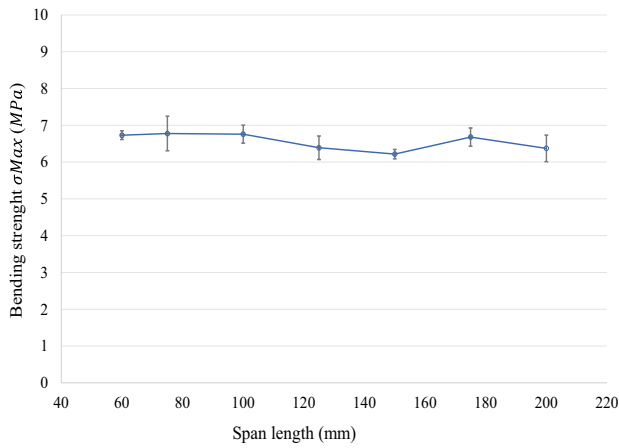
On a macroscopic scale, these behaviors will result in a disparity of the deformations on a specimen or structure which will depend on the level of the stresses which will be reached locally, the test conditions, the homogeneity of the composition, and the printing direction, etc. The strain fields  $\epsilon_{xx}$  obtained by the DIC for a loading state before fracture at different span lengths (100, 150, and 200 mm), presented in Fig. 9, illustrate this well. To facilitate the comparison of these measurements made on the elastic phase of the curves (phase 3), the scale of the deformation iso-values was kept fixed.

As expected, we observe the presence of tensile strain on the upper part of the test specimens and of compression on the lower part delimited by horizontal green lines on the images which is positioned at the middle of the specimens (Fig. 9). The location of the neutral plane which is characterized by zero bending stress is function of modular ratio  $ET/EC$  (where  $ET$  and  $EC$  are tensile modulus and compression modulus respectively) [27]. The equal distances from neutral plane to top and bottom of the specimen indicate hence that the tensile modulus is equal to compression modulus. This symmetry of behavior can be explained by the porous nature of structure that allows the sliding of sand in compressed section without compaction. For all the tested configurations, the strain distribution is consistent, where the high strains are measured at the center of the specimens where the stresses are higher. The maximum values of the strains, both in

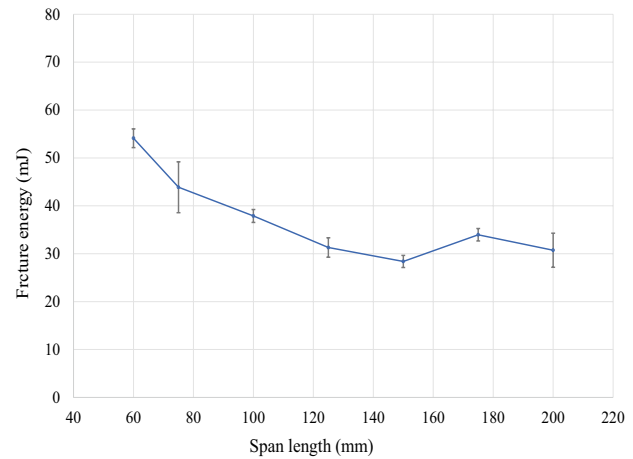
**Table 2** Results of the mechanical parameters

Span length (mm)	Maximal strength		Elastic modulus		Fracture energy (MJ)	
	Average (MPa)	Standard deviation (%)	Average (MPa)	Standard deviation (%)	Average (MJ)	Standard deviation (%)
60	$6.73 \pm 0.12$	1.76	$308.64 \pm 30.23$	9.80	$54.11 \pm 1.96$	3.63
75	$6.78 \pm 0.47$	6.95	$504.54 \pm 17.82$	3.53	$43.88 \pm 5.31$	12.11
100	$6.76 \pm 0.25$	3.63	$832.02 \pm 56.46$	6.79	$37.88 \pm 1.34$	3.54
125	$6.39 \pm 0.32$	5.01	$1063.70 \pm 56.81$	5.34	$31.30 \pm 2.03$	6.49
150	$6.22 \pm 0.13$	2.09	$1372.41 \pm 6.91$	0.50	$28.39 \pm 1.26$	4.45
175	$6.68 \pm 0.25$	3.75	$1631.10 \pm 45.78$	2.81	$33.96 \pm 1.30$	3.82
200	$6.37 \pm 0.36$	5.67	$1821.02 \pm 5.17$	0.28	$30.74 \pm 3.56$	11.57





**(a) Bending strength**



**(b) Fracture energy**

**Fig. 6** Bending strength **(a)** and fracture energy **(b)** evolution as function of span length

compression and in tensile, are measured in the case of weak span length, i.e., at 100 mm, and are in sections located on the central part of the tested specimen. This is consistent because the forces, and therefore the stresses given that the section is constant, are greater for low span length tests (Fig. 5).

If we look to the symmetry of the measurements, we observe that the strains located on the same section at identical distances from the central axis of the specimen

are not identical. This is illustrated by the values reported in Fig. 9 which were measured on the ends of the central sections, where the pin applies the bending force, represented by the vertical green line on the images. We observed in the case of specimens having a span length of 100 mm, where the difference is significant, that the tensile strain (0.133%) has an absolute value greater than that of the compression (−0.1%). This can be attributed to the local disparity in material composition and stresses

**Fig. 7** Load–displacement curve of cyclic bending test performed at a span length of 200 mm

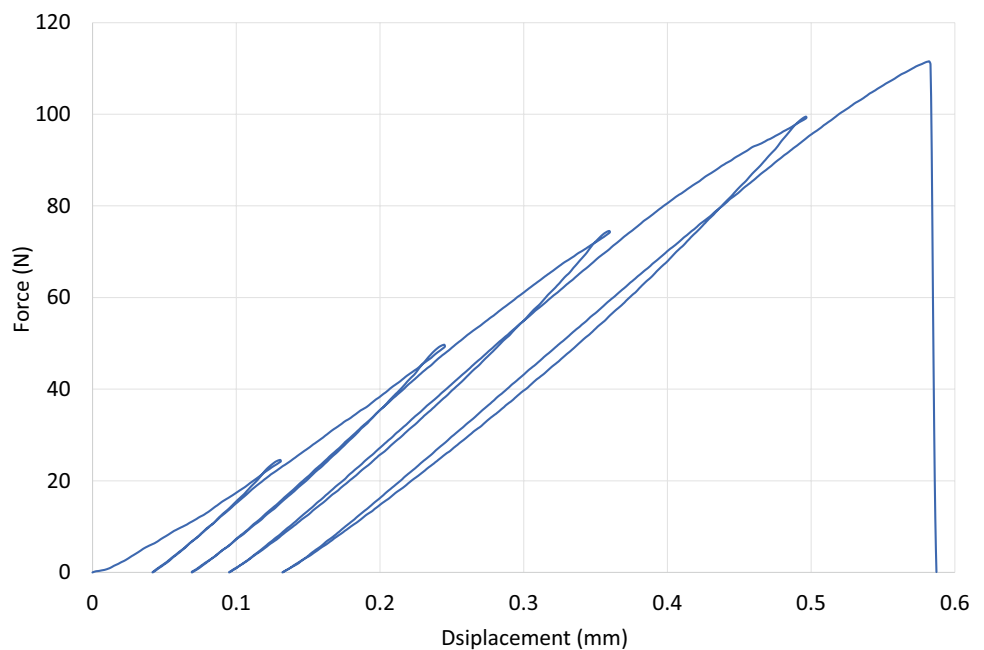
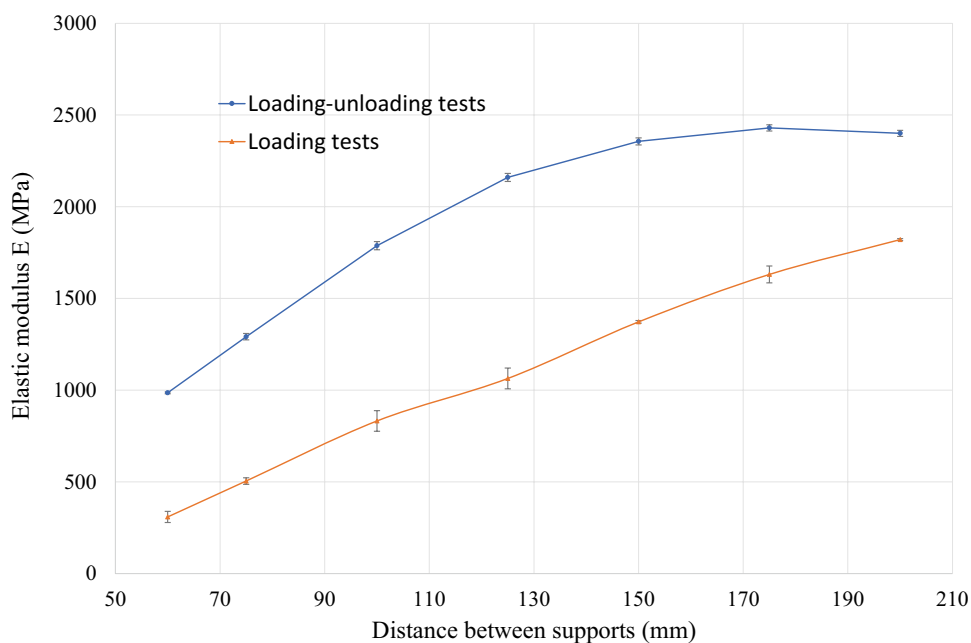


**Fig. 8** Elastic modulus evolution as function of span length



but also to the effect of the onset of fracture initiation since these measurements were made just before failure.

To investigate this, measurements of the deformation fields were carried out at loading states well before failure. An example is shown in Fig. 10 for tests with span length of 200 mm. Strain distributions according to horizontal and vertical lines (green lines on the figure) were extracted and plotted on the curves under the image.

The symmetry of the strain's measurements remains correct in both directions with respect to the axes of symmetry of the specimen. The difference between the deformations measured, at the ends of the sections considered in the two directions (Fig. 10), remains small and acceptable. The evolution trend of the strains between the ends of the sections, both vertical and horizontal, also remains correct. However, these evolutions are not linear according to the vertical sections and are very disturbed and not smooth for the horizontal sections. This effect is attributed to the local variability of the printed sand leading to a variability of local stresses and specifically that of shear. That is confirmed by the measurements of shear strains ( $\epsilon_{xy}$ ) representative of the state of the shearing stresses, where one notes this variability which is more pronounced in the case of small span length where the level of stresses is more important like for normal stresses (Fig. 11). The results of shear strain distribution obtained with span length equal to 100 mm indicate that the bending specimen undergoes high level of shear stress that requires considering the shear rigidity which

is neglected by the used Euler–Bernoulli Beam equations. The Timoshenko beam theory must be used to get exact solution when bending is combined with shear [28]. The axial strain and the shear strain are function of deflection, horizontal displacement, and rotation of cross-section [29], whereas in our study the rotation of cross-section is not considered. For this reason, the elastic modulus values calculated for span length less or equal to 150 mm are different than the values determined for span lengths equal to 175 mm and 200 mm.

To conclude, even if the measured strain fields remain consistent with what can be expected for a bending test, they are still marked by local variations due to the homogeneity of the printed sand. When the span length increases, the distribution of the strains becomes more homogeneous, both locally and globally, and the strain values tend to fall (Figs. 9 and 11). This constitutes an additional motivation to carry out the tests with high span-to-thickness value, thus making it possible to overcome the effect of local phenomena.

The second parameter used in this study is the testing speed. Tests were performed with two speeds of the cross-head tensile machine, which are 5 mm/min and 0.05 mm/min. This represents a factor of 100, which is sufficient to identify the potential effect of the strain rate on the mechanical behavior of the printed sand. The span length was 150 mm. Another batch of samples, different from those tested previously, was used to respect the conditioning constraints established at the beginning, that is, testing samples 24 h after production.

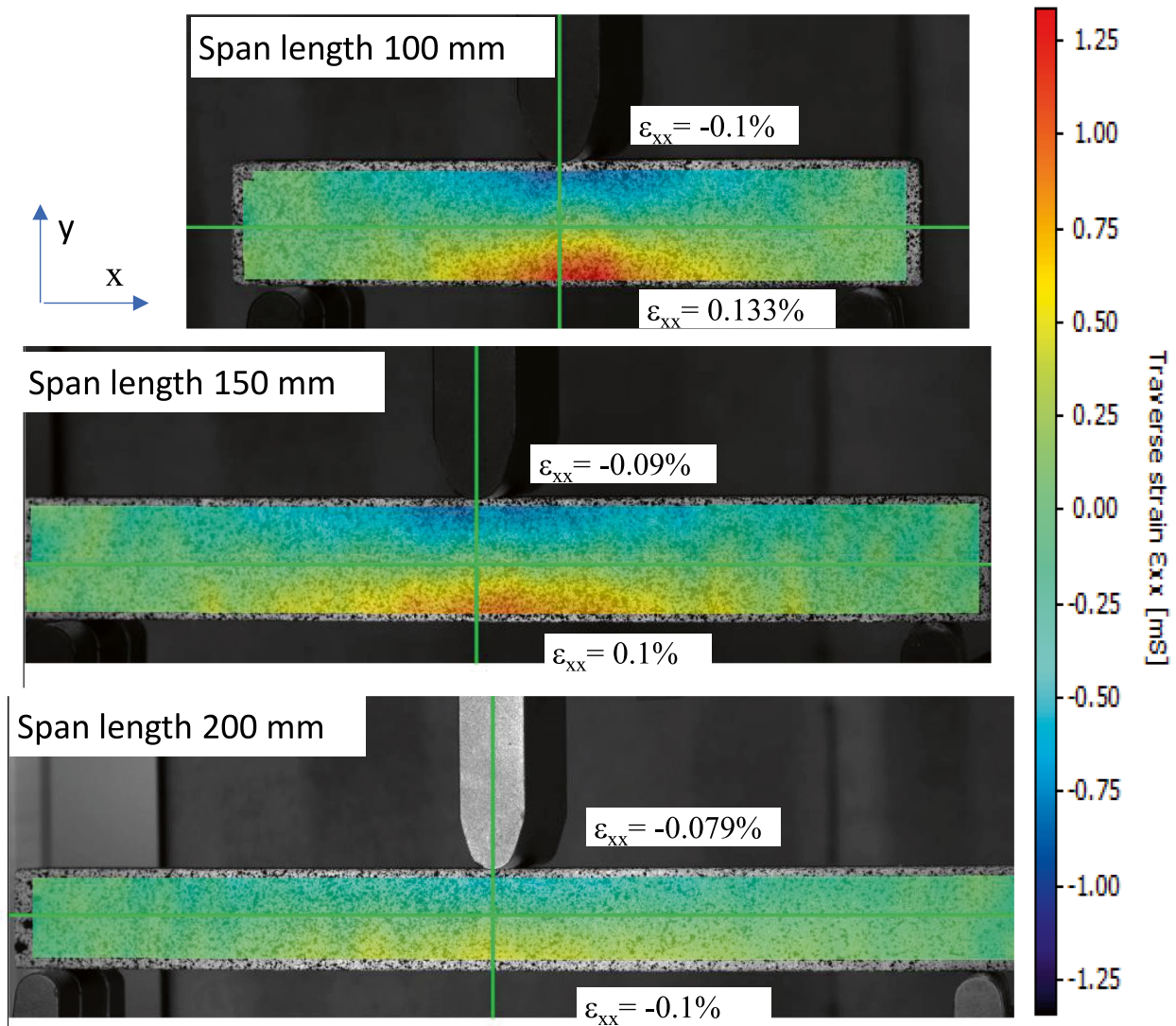


**Fig. 9** Stain field ( $\epsilon_{xx}$ ) measurements before fracture at different span lengths

The comparison of the behaviors is illustrated in Fig. 12 where only one curve per configuration is plotted for better readability. Results of the mechanical parameter function of the testing speed are given in Table 3. Thus, we observe that tests performed at 5 mm/min (Table 3) exhibit the same results than those obtained previously for the tests with different span length on another batch of sample (Table 2). This therefore confirms the repeatability of the results and the robustness of the characterization protocol as well as the reproducibility of the 3D printing process used in this study.

The decrease of displacement rate from 5 to 0.05 mm/min leads to a decrease of maximal bending strength value of about 26%, whereas the elastic modulus only drops by

3.2%, which remains largely within the dispersion of the results, which is between 2 and 6% for the two configurations (Table 3). The ultimate stress, and therefore the dissipated energy, evolves as a function of the strain rate, while the elastic modulus is not affected.

Moreover, the force–displacement curves for the tests performed at high displacement speeds are characterized by several load drops while those at low speed are quite smooth (Fig. 12). This effect may be due to the potential effect of sliding between the sample and the device pins or even progressive decohesion of sand particles. We can therefore conclude that the effect of the strain rate is not significant on the elastic parameters of the printed sand while the breaking stress increases according to the testing speed.

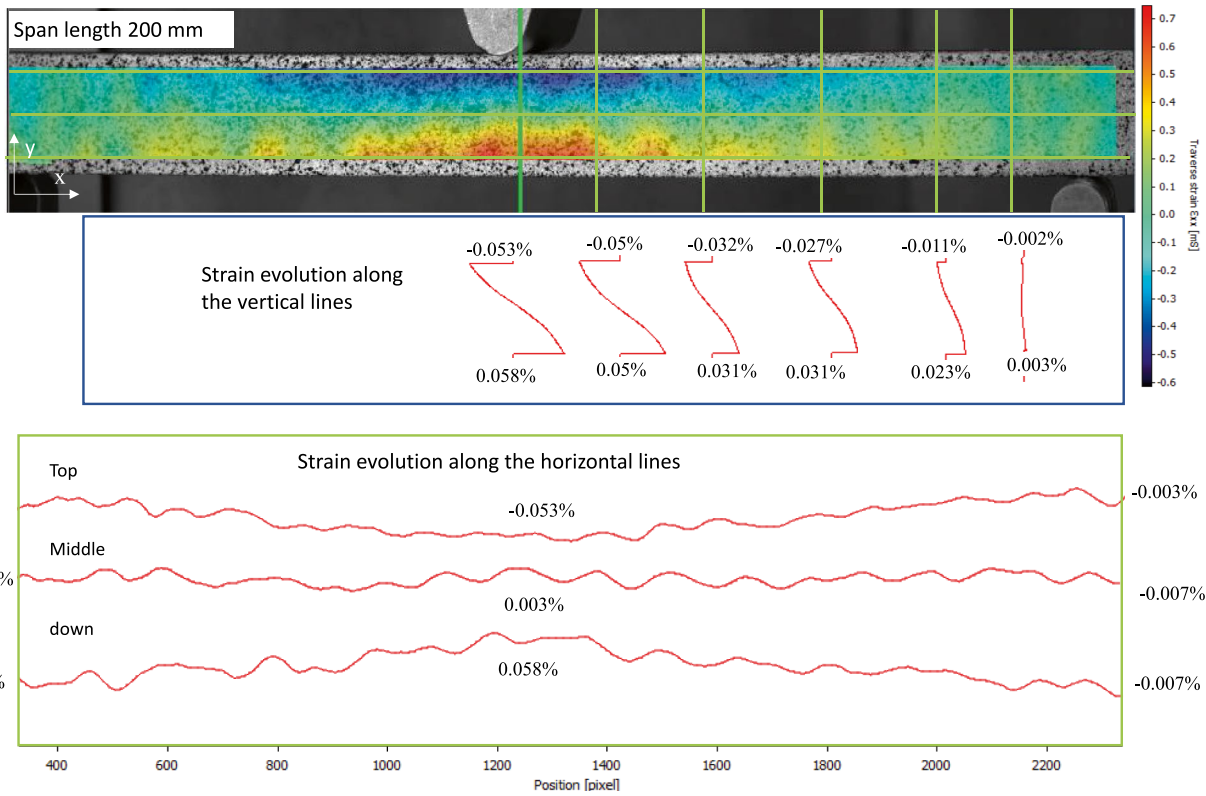


**Fig. 10** Strain ( $\epsilon_{xx}$ ) distribution along sections of the specimens with a span length of 200 m

**Fig. 11** Shear strain field ( $\epsilon_{xy}$ ) measurements before fracture point at different span lengths

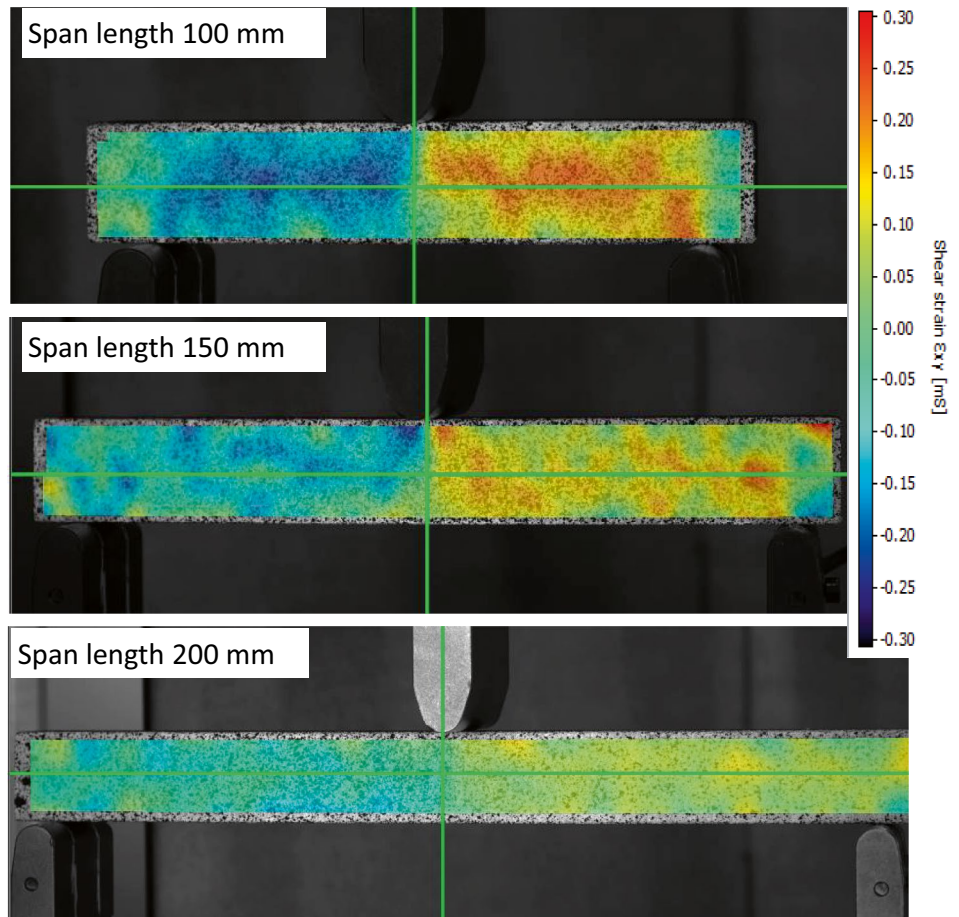


**Fig. 12** Load–displacement curves as function of testing speed

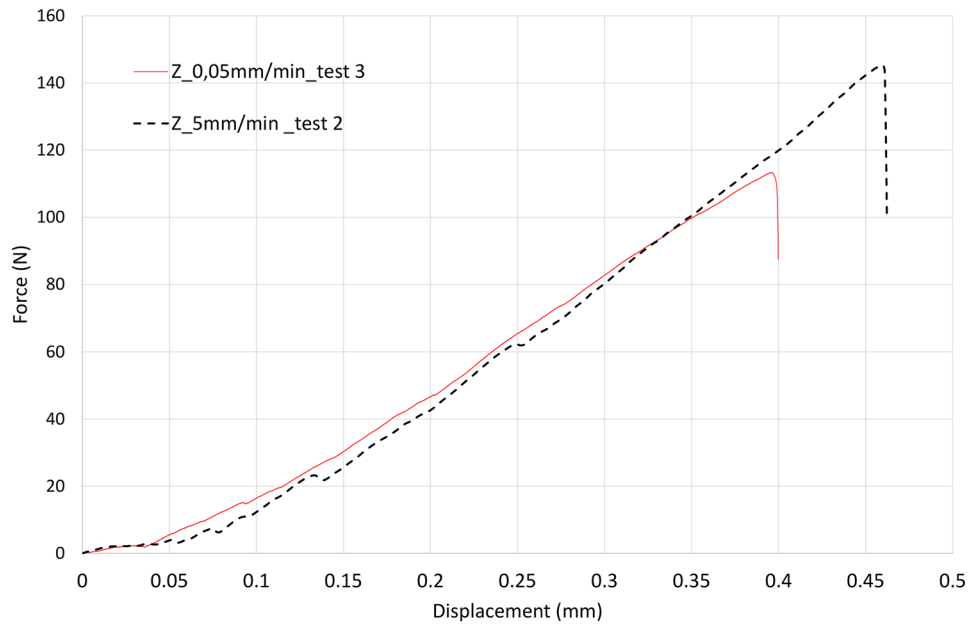


**Table 3** Results of the mechanical parameter function of the testing speed

3	Parameter	Test 1	Test 2	Test 3	Average	Standard deviation (%)
5 mm/min	Maximal stress (MPa)	6.24	6.09	6.21	6.18 ± 0.08	1.29%
	Young modulus (MPa)	1348.19	1363.90	1401.70	1371.27 ± 27.5	2.01%
0.5 mm/min	Maximal stress (MPa)	4.44	4.53	4.67	4.55 ± 0.11	2.51%
	Young modulus (MPa)	1422.05	1271.36	1289.25	1327.56 ± 82.33	6.20%

### 4 Conclusion

This study proposes to evaluate the effect of span-to-thickness (specimen length/specimen height) and strain rates on the printed sand mechanical behavior during three-point bending tests instrumented with optical measurements. The DIC measurements highlighted the presence of a local crushing at the specimen/pin contacts, due to the Hertz pressure, that affects the onset of the behavior. To overcome or limit this phenomenon, it would be necessary to favor the use of loading and supporting pins having a large diameter.

The assessed flexural strength of sand printed specimens under three-point bending is not affected by span length value contrary to the elastic modulus, which increases with span length. This evolution was observed both during the simple bending test, but without value stabilization, and with the loading–unloading, more reliable method that gave rise to higher results with a stabilization of the elastic modulus values after a span-to-thickness value of 8. The fracture energy, for its part, decreased and reached a plateau starting after a span-to-thickness ratio of 5.7. Moreover, when the span length

increases, the DIC measurements showed that the distribution of the strain fields becomes more homogeneous both locally and globally. Therefore, for the characterization of the intrinsic elastic properties of printed sand using three-point bending tests, it will be appropriate to use a loading–unloading test and to choose a span-to-thickness greater than 8 to overcome parasitic phenomena and coupling with shear behavior. The increase of the strain rate, in the value range used, leads to an increase of the breaking stress. Hence, for the determination of the intrinsic stress of printed sands, it would be necessary to choose the strain rate close to conditions during casting for the intended application.

Future research will focus on the study of mechanical behavior at high temperatures for relevant sizing of the foundry molds and cores and to make simulations of the molding process more robust.

**Acknowledgements** The authors are thankful to the company 3D Metal Industrie for providing sand printed samples.

**Funding** This work was supported by French Région Grand Est (grant number D201507798), the European Union (grant number

D201507799), and UIMM (grant number 13–2015) within the Chair MATUR.

**Availability of data and material** Not applicable.

**Code availability** Not applicable.

## Declarations

**Ethics approval** The authors obliged to all the rules regarding the ethic in publication.

**Consent to participate** Not applicable.

**Consent for publication** The authors consent the policy of publication in *The International Journal of Advanced Manufacturing Technology*.

**Conflict of interest** The authors declare no competing interests.

## References

- Bassoli E, Gatto A, Iuliano L, Violante MG (2007) 3D printing technique applied to rapid casting. *Rapid Prototyping Journal* 13(3):148–155. <https://doi.org/10.1108/13552540710750898>
- Gibson I, Rosen D, Stucker B (2015) *Binder jetting*. Addit Manuf Technol. Springer, New York, NY, pp. 205–218
- Sama SR, Wang J, Manogharan G (2018) Non-conventional mold design for metal casting using 3D sand-printing. *J Manuf Process* 34:765–775. <https://doi.org/10.1016/j.jmapro.2018.03.049>
- Shangguan H, Kang J, Deng C, Hu Y, Huang T (2017) 3D-printed shell-truss sand mold for aluminum castings. *J Mater Process Technol* 250:247–253. <https://doi.org/10.1016/j.jmatprotec.2017.05.010>
- Shangguan H, Kang J, Yi J, Zhang X, Wang X, Wang H, Huang T (2018) The design of 3D-printed lattice-reinforced thickness-varying shell molds for castings. *Materials* 11(4):535. <https://doi.org/10.3390/ma11040535>
- Sama SR, Badamo T, Lynch P, Manogharan G (2019) Novel sprue designs in metal casting via 3D sand-printing. *Addit Manuf* 25:563–578. <https://doi.org/10.1016/j.addma.2018.12.009>
- Walker J, Harris E, Lynagh C, Beck A, Lonardo R, Vuksanovich B, Thiel J, Rogers K, Conner B, Mac Donald E (2018) 3D printed smart molds for sand casting. *Int J Metalcast* 12:785–796. <https://doi.org/10.1007/s40962-018-0211-x>
- Upadhyaya M, Sivarupana T, El Mansori M (2017) 3D printing for rapid sand casting—a review. *J Manuf Process* 29:211–220. <https://doi.org/10.1016/j.jmapro.2017.07.017>
- Low ZX, Chua YT, Ray BM, Mattia D, Metcalfe IS, Patterson DA (2017) Perspective on 3D printing of separation membranes and comparison to related unconventional fabrication techniques. *J Membr Sci* 523:596–613. <https://doi.org/10.1016/j.memsci.2016.10.006>
- Sachs E, Cima M, Cornie J (1990) Three-dimensional printing: rapid tooling and prototypes directly from a CAD model. *CIRP Ann Manuf Technol* 39(1):20–204. [https://doi.org/10.1016/S0007-8506\(07\)61035-X](https://doi.org/10.1016/S0007-8506(07)61035-X)
- Motoyama Y, Inoue Y, Saito G, Yoshida M (2013) A verification of the thermal stress analysis, including the furan sand mold, used to predict the thermal stress in castings. *J Mater Process Technol* 213(12):2270–2277. <https://doi.org/10.1016/j.jmatprotec.2013.06.024>
- Marumoto N, Kashimura H, Yoshida K, Toyoda T, Okane T, Yoshida M (2016) Dynamic measurements of the load on gray cast iron castings and contraction of castings during cooling in furan sand molds. *J Mater Process Technol* 237:48–54. <https://doi.org/10.1016/j.jmatprotec.2016.05.012>
- Bernhard JS, Kerber H, Schumacher P (2016) Foundry sand core property assessment by 3-point bending test evaluation. *J Mater Process Technol* 237:188–196. <https://doi.org/10.1016/j.jmatprotec.2016.06.010>
- Sivarupan T, Balasubramani N, Saxena P, Nagarajan D, El Mansori M, Saloni K, Jolly M, Dargusch MS (2021) A review on the progress and challenges of binder jet 3D printing of sand moulds for advanced casting. *Addit Manuf* 40:101889. <https://doi.org/10.1016/j.addma.2021.101889>
- Khandelwal H, Ravi B (2015) Effect of binder composition on the shrinkage of chemically bonded sand cores. *Mater Manuf Process* 30(12):1465–1470. <https://doi.org/10.1080/10426914.2014.994779>
- Khandelwal H, Ravi B (2016) Effect of molding parameters on chemically bonded sand mold properties. *J Manuf Process* 22:127–133. <https://doi.org/10.1016/j.jmapro.2016.03.007>
- Matthew A (2019) Perras, Daniel Vogler, Compressive and tensile behavior of 3D-printed and natural. *Transp Porous Media* 129:559–581
- Voglera D, Walsh SDC, Dombrovski E, Perras MA (2017) A comparison of tensile failure in 3D-printed and natural sandstone. *Eng Geol* 226:221–235
- Mitra S (2019) Experimental and numerical characterization of functional properties of sand molds produced by additive manufacturing (3D printing by jet binding) in a fast foundry, Phd thesis, Ecole Nationale Supérieure, France
- Coniglio N, Sivarupan T, El Mansori M (2018) Investigation of process parameter effect on anisotropic properties of 3D printed sand molds. *Int J Adv Manuf Technol* 94(5–8):2175–2185. <https://doi.org/10.1007/s00170-017-0861-5>
- Vaezi M, Chua CK (2011) Effects of layer thickness and binder saturation level parameters on 3D printing process. *Int J Adv Manuf Technol* 53(1–4):275–284. <https://doi.org/10.1007/s00170-010-2821-1>
- Dana HR, El Mansori M (2020) Mechanical characterisation of anisotropic silica sand/furan resin compound induced by binder jet 3D additive manufacturing technology. *Ceram Int* 46:17867–17880. <https://doi.org/10.1007/s11242-018-1153-8>
- Del Giudice L, Vassiliou MF (2020) Mechanical properties of 3D printed material with binder jet technology and potential applications of additive manufacturing in seismic testing of structures. *Addit Manuf* 36:101714. <https://doi.org/10.1016/j.addma.2020.101714>
- Mitra SR, de Castro A, El Mansoria M (2019) On the rapid manufacturing process of functional 3D printed sand molds. *J Manuf Process* 42:202–212. <https://doi.org/10.1016/j.jmapro.2019.04.034>
- AFS (1962) *Molding methods and materials*, 1st edn. American Foundrymen's Society, Des Plaines, Illinois
- VDG-Merkblatt P 71 (1999) Biegefestigkeit von warmhärtenden kunstharzgebundenen feuchten Formstoffen. VDG. Düsseldorf
- Chamis CC (1974) Analysis of the three-point-bend test for materials with unequal tension and compression properties NASA TN D-7572
- Fogang V (2020) Timoshenko beam theory exact solution for bending, second-order analysis, and stability. Preprints 2020110457. <https://doi.org/10.20944/preprints202011.0457.v1>
- Dao-KuiLi X-F (2016) Large deflection and rotation of Timoshenko beams with frictional end supports under three-point bending. *Comptes Rendus Mécanique* 344(8):556–568

**Publisher's note** Springer Nature remains neutral with regard to jurisdictional claims in published maps and institutional affiliations.